



HAL
open science

Nonequilibrium in Thermal Plasmas with Applications to Diamond Synthesis

C. Kruger, T. Owano, C. Laux, R. Zare

► **To cite this version:**

C. Kruger, T. Owano, C. Laux, R. Zare. Nonequilibrium in Thermal Plasmas with Applications to Diamond Synthesis. *Journal de Physique IV Proceedings*, 1997, 07 (C4), pp.C4-67-C4-92. 10.1051/jp4:1997406 . jpa-00255562

HAL Id: jpa-00255562

<https://hal.science/jpa-00255562>

Submitted on 4 Feb 2008

HAL is a multi-disciplinary open access archive for the deposit and dissemination of scientific research documents, whether they are published or not. The documents may come from teaching and research institutions in France or abroad, or from public or private research centers.

L'archive ouverte pluridisciplinaire **HAL**, est destinée au dépôt et à la diffusion de documents scientifiques de niveau recherche, publiés ou non, émanant des établissements d'enseignement et de recherche français ou étrangers, des laboratoires publics ou privés.

Nonequilibrium in Thermal Plasmas with Applications to Diamond Synthesis

C.H. Kruger, T.G. Owano, C.O. Laux and R.N. Zare*

Mechanical Engineering Department, High Temperature Gasdynamics Laboratory, Stanford University, Stanford, California 94305, U.S.A.

** Chemistry Department, Stanford University, Stanford, California 94305, U.S.A.*

Abstract - Atmospheric pressure plasmas are frequently considered to be in local thermodynamic equilibrium due to the high frequency of collisional processes which drive the plasma state towards a Maxwell-Boltzmann equilibrium. However, various forms of thermodynamic, ionizational, and chemical nonequilibrium have been demonstrated and investigated in atmospheric pressure plasma environments over the last several years, and the nonequilibrium behavior of such systems can be quite significant. The investigation, understanding, and exploitation of atmospheric pressure nonequilibrium plasma chemistry is necessary to the further expansion of plasma-based systems into mainstream manufacturing and processing applications. Several experimental programs to investigate the fundamental processes of atmospheric pressure nonequilibrium plasma chemistry, and the application of this nonequilibrium to various chemical systems have been undertaken in our laboratories. The results of these investigations have shed light on the kinetics behind various forms of atmospheric pressure nonequilibrium chemistry, and provided insights into the beneficial control of nonequilibrium plasma chemistry for processing applications.

1. INTRODUCTION

Nonequilibrium chemistry in atmospheric and near atmospheric pressure plasmas has emerged as an important factor in the understanding and design of plasma processing systems. Although atmospheric pressure thermal plasmas have been regarded in the past as equilibrium systems for which equilibrium diagnostic interpretations are suitable, and have been used primarily for high-enthalpy processes, recent research has shown that both naturally occurring and induced nonequilibrium chemistry can dramatically change the properties and capabilities of these plasmas. This nonequilibrium plasma chemistry offers challenges to current diagnostic techniques and their interpretation, as well as the opportunity to expand the range and scale of current plasma processing systems. The benefits of nonequilibrium plasma chemistry have been known and applied in low pressure plasma processing systems, and in fact those particular properties are responsible for making many of these processes possible (such as anisotropic etching in semiconductor manufacturing). Recent efforts to bring the unique capabilities of plasma processing into mainstream manufacturing have been hampered by the need to accomplish these processes on larger scales, with higher throughput, and at atmospheric or near atmospheric pressure.

In this paper we will illustrate our recent research in several plasma systems for purposes of fundamental radiation and kinetic studies, thermal plasma CVD, and aerothermal applications. In these studies we have encountered various forms of electronic, vibrational, ionizational, and chemical nonequilibrium that required experimental characterization using a variety of complementary diagnostic techniques ranging from emission spectroscopy to advanced laser-based diagnostics. We will describe these techniques and discuss various models that have been developed and applied to interpret and predict the observed nonequilibrium. We will demonstrate how this new understanding of nonequilibrium behavior can be applied to the synthesis of advanced materials, and to the improvement of nonequilibrium radiation models. Finally, we will present preliminary results from a novel plasma processing technique that selectively enhances desirable nonequilibrium chemistry by means of targeted

energy addition to the free electrons. The combination of appropriate plasma diagnostic techniques and detailed interpretive tools is essential for the further understanding of nonequilibrium plasma environments and the advancement of plasma processing technology.

2. EXPERIMENTAL FACILITIES

The research described here has been carried out in the laboratories of the High Temperature Gasdynamics Laboratory, Department of Mechanical Engineering, at Stanford University. In this laboratory, we currently operate two large-scale atmospheric pressure plasma facilities, one low pressure reactor, and several state-of-the-art laser-based diagnostic facilities. In this section we will briefly review these facilities.

2.1 RF Plasma Torch Facility

The RF plasma torch facility is centered around a 50 kW TAFE model 66 RF induction plasma torch, powered by a LEPEL model t-50-3 power supply operating at a frequency of 4 MHz. The torch head itself (shown schematically in Figure 2.1) consists of a 5-turn copper induction coil (mean radius 8.6 cm and height 8.6 cm) surrounding a 3 mm thick quartz tube (inner radius approx. 7.6 cm) and encased in a Teflon body with brass end plates. Overall size of the torch head is approximately 15 cm diameter and 35 cm height. Deionized cooling water is circulated around the load coil in the annular region between the Teflon body and the inner quartz tube. This provides cooling for both the load coil and the inner quartz tube which contains the generated plasma. Deionized water is used to prevent electrical breakdown between adjacent coils and to limit corrosion and mineral deposits within the cooling system. Copper exit nozzles of 0.5, 1.27, 2.0, 2.54, 3.81, 5.0, and 7.0 cm exit diameter can be utilized at the top of the upward firing torch (with the nozzle exit being approximately 11 cm above the uppermost coil) to provide flowing plasmas of various size and velocity.

The induction torch can operate completely on gases such as argon, air, and nitrogen as well as mixtures involving trace species such as methane, hydrogen, and oxygen. Atmospheric pressure plasmas at temperatures up to 10,000K can be generated, with soft vacuum and super-atmospheric operation also possible with modification. The torch, being relatively large, provides for more realistic conditions not dominated by wall effects, but at the same time is compatible with university-scale research conducted by Ph.D. students. Several flow reactors can also be used in conjunction with the plasma torch. These flow reactors consist of a double walled, water cooled, synthetic fused silica or brass test section (also shown schematically in Figure 2.1) mounted on the exit nozzle of the plasma torch. There are several sizes currently in use, varying from 1 to 7cm in diameter, with flow lengths from approximately 5 cm to 100 cm. The quartz test sections consist of approximately 2 mm thick walled synthetic fused silica tubes (grade GE214 selected for minimum surface defects and maximum smoothness) separated by an approximately 2 mm thick annular water cooling passage. This arrangement prevents entrainment of room air into the flowing plasma as well as providing almost complete optical access to the plasma. The brass test sections are also of a double-walled, water-cooled design, but are modular in construction and can be assembled to any length desired. Without the test section in place, the luminous tail flame of the torch is quenched by room air entrainment within approximately 8-10 cm for the highest power argon cases, and thus the test sections enable the plasma to flow a much longer distance in a relatively well controlled environment.

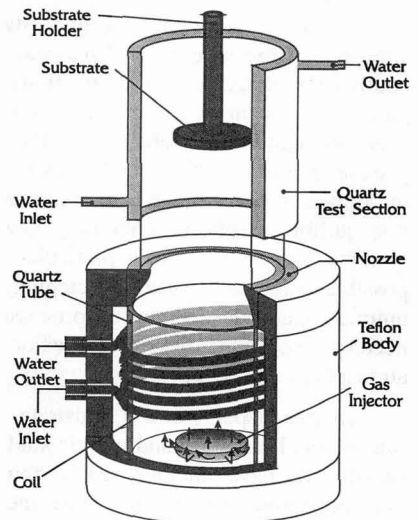


Figure 2.1 Schematic cross-section of torch head.

In addition to the plasma torch itself, the facility is well equipped for spectroscopic diagnostics. Several, multi-level optical tables, two monochromators, PMTs, optics, translators, and an optical chopper / lock-in amplifier combination coupled to a dedicated computer permit study of the plasma by emission spectroscopy. The facility is also complemented by a state-of-the-art laser diagnostic facility described below.

2.2 DC Arcjet Facility

The DC arcjet facility is based around a 150 kW DC arcjet (shown schematically in Figure 2.2). The DC arcjet facility is capable of providing uniform, moderate to high speed atmospheric pressure plasma flows, at temperatures up to approximately 8000 K. The arcjet itself is a Thermal Dynamics Model F-5000 swirl stabilized direct current arcjet, with up to 200 kW of electrical power available from three rectifier banks. It utilizes a molten spot tungsten cathode and a water-cooled copper anode/nozzle. The arcjet typically operates on argon, with process gases injected into the plasma in a small plenum below the arcjet exit. The mixture plasma is the directed through an interchangeable nozzle into the process reactor test section. The interchangeable nozzle design allows for varying exit diameters and thus varying plasma velocities. It is important to note that this plasma/nozzle design provides a uniform plasma flow over the substrate in contrast to conventional configurations of DC arcjets for plasma synthesis.

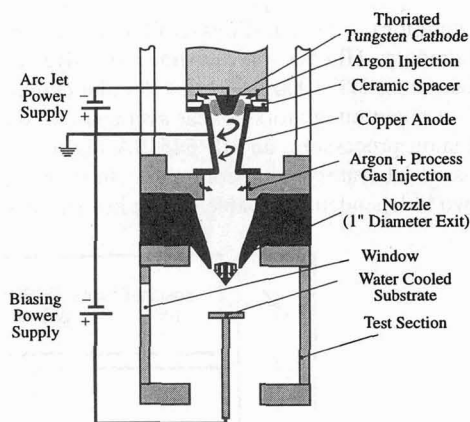


Figure 2.2 Schematic of DC arcjet.

Inside the process reactor test section, substrates are typically mounted in a stagnation point flow geometry, perpendicular to the oncoming plasma. The substrate is separated from its water-cooled holder by means of an adjustable thickness insulator, thus giving control of the substrate temperature, which is monitored pyrometrically through a cooled window. The substrate can be biased with respect to the arcjet and plasma by means of a separate power supply. In preliminary discharge experiments this biasing has been accomplished using a bank of four Kepco Model ATE 100-10M power supplies in parallel, each rated at 100 V - 10 A.

2.3 Hot-Filament Reactor System

The hot-filament reactor is shown schematically in Figure 2.3, and consists of a 5-way stainless steel cross 4 inches in diameter. A two-stage mechanical pump (E2M40, Edwards) is used to evacuate the chamber to the minimum pressure of 4×10^{-3} Torr. Inside this reactor, a tungsten filament is positioned horizontally inside the chamber using two tungsten posts, 4 cm long and 1.5 mm in diameter, mounted on water-cooled copper electrodes. The tungsten filament is typically 20 mm long and 200 μm in diameter, and is resistively heated with dc current while its temperature is monitored with a disappearance pyrometer (Pyro Micro-Optical Pyrometer). Substrates can be mounted near the filament via a similar post support system, and are typically made of a molybdenum strip (4 mm x 20 mm x 250 μm). The substrate is also resistively heated via an AC power source. The substrate temperature is monitored with a K Type thermocouple which is welded to the rear surface of the substrate, and also by an infra-red optical pyrometer (Minolta Cyclops).

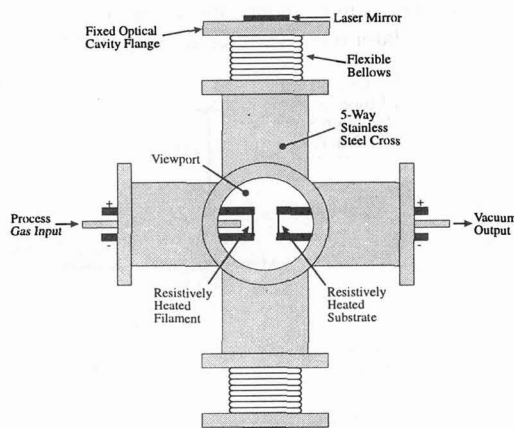


Figure 2.3 Schematic of the Hot-Filament Reactor.

2.4 Visible/UV Laser Facility

A complete nano-second laser facility is currently in operation at the RF plasma torch facility, and is comprised of a Spectra-Physics DCR-4G Nd:YAG laser (modified for temperature stabilized 20 Hz operation), a Spectra-Physics PDL-2 dye laser, a Spectra-Physics WEX frequency doubler and mixer, a Lumonics HD-500 narrow linewidth dye laser modified with a special Bethune cell amplifier, and a Lumonics HT-1000 frequency doubler (Figure 2.4). Associated equipment for the laser facility includes four gated integrators/boxcar averagers, a four channel digital delay/pulse generator, fast pre-amplifiers, analog processors, an HP 54510A digitizing oscilloscope, associated optics, and a dedicated Pentium based laboratory microcomputer. In its present configuration, the laser system is capable of delivering two independently tunable source beams for simultaneous spectroscopic interrogations.

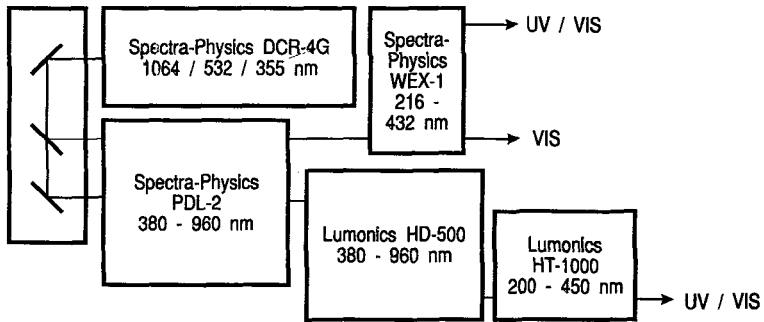


Figure 2.4 Schematic of laser facility.

2.5 Infra-Red OPO Laser Facility

We have also developed an infra-red Optical Parametric Oscillator (OPO) laser facility (shown schematically in Figure 2.5). These infra-red OPO systems have only recently become commercially available and represent instrumentation that exists at only a few facilities nationwide. The infrared OPO system produces near transform-limited nanosecond pulses (0.017 cm^{-1} bandwidth) that are continuously tunable from 1.5 to $10 \mu\text{m}$, with pulse energies varying from approximately 10 mJ in the near infrared to approximately 100 μJ at $10 \mu\text{m}$. The laser system consists of an injection seeded Nd:YAG pump laser (Continuum Powerlite 8000) coupled to an optical parametric master oscillator operated in the near-infrared followed by two successive parametric converter stages (Continuum MIRAGE 3000) and a difference frequency generation stage to extend the accessible wavelength range to $10 \mu\text{m}$ (Continuum MX-1). The single mode operation of the laser system is assured by continuous monitoring of the master oscillator and use of an actively stabilized cavity.

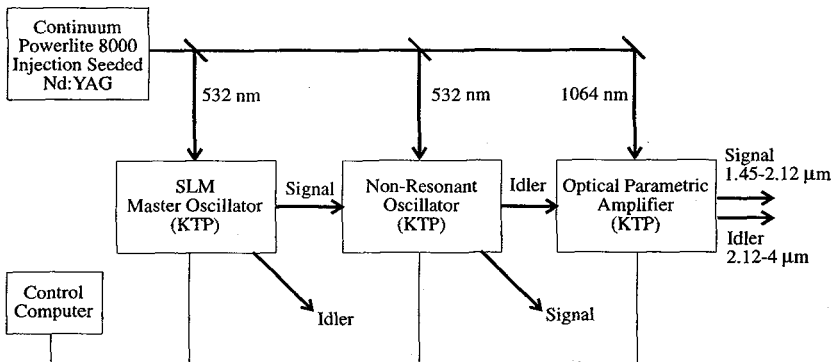


Figure 2.5 Schematic of the infra-red OPO laser facility.

3. INVESTIGATIONS AND DIAGNOSTICS OF NONEQUILIBRIUM PLASMA CHEMISTRY

In recent years, we have investigated the nature and chemistry of atmospheric pressure plasmas. In this effort, fundamental information on the plasma state, excitation temperatures, electron densities, radiation escape, recombination rates, and electronic quenching of excited levels have been investigated. The plasmas studied have ranged from simpler noble gas plasmas, to more complex admixtures involving diatomics such as hydrogen and nitrogen, to very complex reacting environments such as air plasmas and the diamond producing argon-hydrogen-methane system. As part of these fundamental investigations, we have developed and applied advanced, laser based diagnostic techniques in order to understand realistic plasma synthesis and plasma processing environments.

3.1 Noble-Gas and Dilute Mixture Plasmas

Atmospheric pressure argon plasmas have been used to investigate the applicability of LTE assumptions to noble gas plasmas of moderate temperatures and electron densities ($< 10,000$ K, 10^{22} m⁻³ respectively). In these experiments, emission diagnostics are used to assess the plasma state at several locations downstream of the excitation source. Absolute line intensities, relative line intensities, and absolute continuum intensities are used to determine electronic state populations, electron density, and associated temperatures. The measurement of excited electronic state populations and electron density allows the applicability of LTE assumptions to be tested at the conditions of interest.

If a plasma is truly in a state of LTE, temperatures describing the absolute and relative electronic level populations, as well as their relation to the density of free electrons, will be the same. Recombining argon plasmas in the temperature and electron density range of 5000 - 8500 K, 10^{20} - 10^{22} m⁻³ respectively, downstream of the inductively coupled plasma torch, have been investigated in this manner and found to exhibit non-LTE behavior.[1, 2] This is due to the relatively slow electron-ion three-body recombination rates. Nevertheless the plasma is found to maintain partial local thermodynamic equilibrium, or PLTE. In this state of PLTE, excited electronic states and free electrons are mutually in partial equilibrium at the Boltzmann temperature T_B , as given by the excited state Saha equation:

$$\frac{n_e^2}{n_j} = \frac{2g_i}{g_j} \left(\frac{2\pi m_e k T_B}{h^2} \right)^{3/2} \exp\left(\frac{-\epsilon_{j\lambda}}{k T_B} \right)$$

where ϵ_{ji} is the ionization energy of the j th excited level, g_i represents the ion partition function, and the other symbols have their usual meaning. The absolute populations of bound and free electrons, however, deviate from LTE with the ground state by a nonequilibrium factor, α , given by:

$$\frac{n_i}{g_i} = \alpha \left(\frac{1}{g_1} \right) \left(\frac{p}{k T_B} \right) \exp\left(\frac{-\epsilon_i}{k T_B} \right)$$

$$\left(\frac{n_e^2}{n_1} \right) = \alpha \left(\frac{2g_i}{g_1} \right) \left(\frac{2\pi m_e k T_B}{h^2} \right)^{3/2} \exp\left(\frac{-\epsilon_i}{k T_B} \right)$$

Although emission measurements allow only confirmation of PLTE in the argon plasmas to electronic levels as low as $j=3$, absorption measurements indicate that PLTE in fact extends to $j=2$ for the range of conditions investigated. Since the partial equilibrium is maintained by collisions between excited electronic states and free electrons, the Boltzmann temperature T_B should agree with the free electron translational temperature T_e . This is supported by detailed collisional-radiative models which show equilibration, at sufficiently high electron densities, between the electron temperature T_e and the Boltzmann slope temperature T_B of high lying bound electronic levels. Analysis of the electron energy equation in the regions downstream of the excitation source indicates relatively small differences between the electron temperature T_e and the heavy particle gas temperature T_g . Detailed investigation of the electron-ion three body recombination coefficient of argon[2] shows it to be insufficiently high to

allow ionizational equilibrium to be maintained for even the slow moving, atmospheric pressure plasmas under study. This emphasizes the importance of understanding recombining plasmas so common in plasma chemistry.

The importance of accurately accounting for deviations from LTE can be illustrated by the interpretation of argon radiative source strength measurements. Measurements of the volumetric radiative source strength of argon[1] are shown in Figure 3.1 as interpreted with the assumption of LTE as opposed to those interpreted taking into account effects of the observed PLTE. Since the bound and free electrons responsible for the radiative emission of the plasma are, for the most part, overpopulated with respect to their LTE values, we can see that the value obtained using LTE assumptions drastically overpredicts the low temperature values of radiative source strength. Also shown in Figure 4.1 are the measurements of Emmons, who made use of LTE arguments in his data reduction, as well as a proposed upper bound curve, based on the argument that the observed radiation must fall off with decreasing temperature at least as fast as a Boltzmann factor corresponding to the population of the second excited level at 13.1 eV. We see in this case that the use of LTE temperatures for determining the plasma state and interpreting measurements is unsatisfactory.

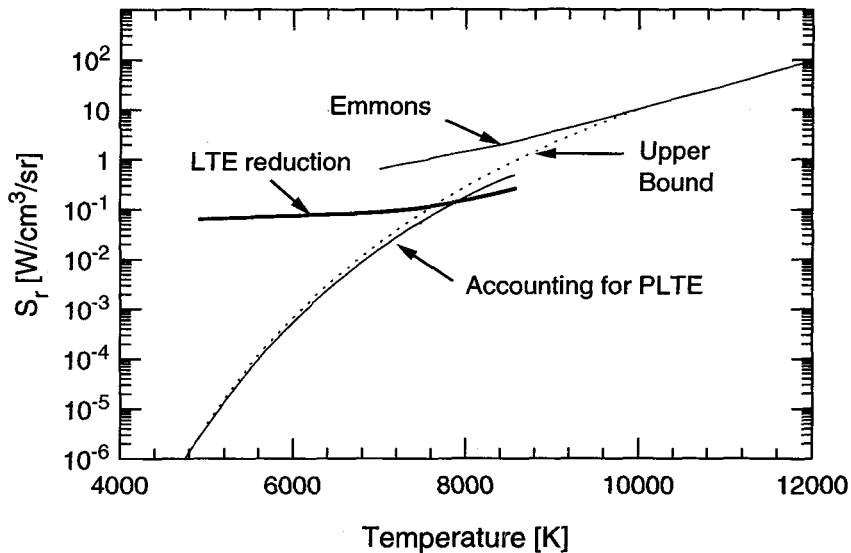
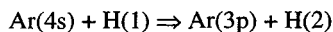


Figure 3.1 Radiative source strength of argon.

As a step toward more complex systems, we have mixed small amounts of nitrogen or hydrogen with argon under conditions similar (but not necessarily identical) to those of the noble-gas experiments. It is found that under conditions where the plasma is still strongly recombining at the test-section exit the presence of the diluent causes marked departures from partial local thermodynamic equilibrium between the bound and free electrons.[3] Typical results are shown in Figure 3.2 where the normalized population of the 4p bound state of argon is shown for varying diluent concentrations. In this Figure, an ordinate value of 1 indicates that the 4p level population is in partial equilibrium with the free electrons, while a value of 0 indicates that the 4p level population is in LTE with the ground state. The decrease of the normalized values from unity as the diluent concentration is increased can be described as quenching of the bound-state populations. This quenching will lower the effective radiation source strength and invalidate PLTE diagnostics, such as the line to continuum temperature method.[4] It seems likely that this quenching results from exothermic exchange reactions such as:



An approximate collisional/radiative model, incorporating four levels of argon and four levels of hydrogen with reactions such as the foregoing, has been successful in interpreting the qualitative behavior shown in Figure 3.2.

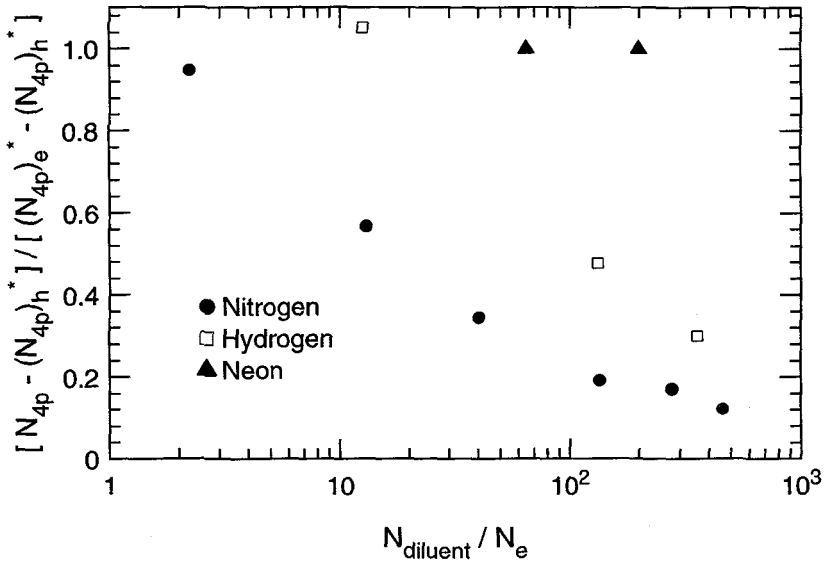


Figure 3.2 Quenching of argon 4p bound electronic level.

An interesting aspect of these experiments is that for the plasmas with nitrogen addition the elevated nonequilibrium electron density appears to be governed not by the usual electron three-body recombination, but rather by the (neutral) recombination of N to N_2 . Based on calculations for these conditions using CHEMKIN[5] with rates from the literature,[6, 7] the concentration of electrons and ionic species is governed by rapid dissociative recombination of N_2^+ and charge exchange between N_2^+ , N^+ , and Ar^+ . According to the CHEMKIN calculations, a partial equilibrium of these reactions establishes the charged-particle concentrations relative to N_2 and N, at least for nitrogen concentrations greater than 1%. More specifically, the CHEMKIN calculations for our conditions support to a good approximation the readily derived result that for partial equilibrium of the dissociative-recombination and charge exchange reactions:

$$\frac{n_e Ar^+ / Ar}{(n_e Ar^+ / Ar)^*} = \frac{N^2 / N_2}{(N^2 / N_2)^*}$$

Here ()^{*} denotes the equilibrium value of the concentration ratio in question. Similar results are obtained for N_2^+ and N^+ , with Ar^+/Ar on the left-hand side replaced by N_2^+/N_2 or N^+/N . It is then the relatively slow recombination of N to N_2 through the test section that maintains and governs the electron-density overpopulation. This effect, if substantiated, may be of considerable importance for a range of plasma chemistry applications where molecular ions are present.

Our experience with recombining inductively coupled plasmas at temperatures below 10,000 K and electron densities below $5 \times 10^{21} \text{ m}^{-3}$ indicates that LTE is not a reliable assumption for plasma diagnostics or plasma modeling. However, for a pure argon plasma partial equilibration between bound and free electrons can be a useful and practical approximation. Under PLTE conditions, electron density and electron temperature must be separately measured, for example, by continuum radiation and the line to continuum temperature method. The validity of this approximation can be checked by accessing several bound states with sufficient energy separation. Under PLTE conditions, the nonequilibrium

radiation source strength is independent of the ground-state density and proportional to the square of the nonequilibrium electron concentration.

Plasmas consisting of mixtures of species including molecules are considerably more complex. The addition of relatively small amounts of nitrogen or hydrogen to a recombining plasma otherwise in PLTE has been shown to produce a quenching of excited state populations, invalidating the usefulness of the PLTE approximation. Under such circumstances, one must resort to direct measurements. Stark broadening and absolute continuum intensities in the visible (as well as other methods) can be used for a direct measurement of the electron density. For the electron temperature, we have used the variation of the recombination radiation intensity with wavelength in the UV.[8] This method assumes only a Maxwellian electron translational velocity distribution function and a satisfactory knowledge of the recombination cross section through the so-called Biberman factor. Application of this method to our well-diagnosed argon plasmas shows good agreement under PLTE conditions with Boltzmann and line to continuum temperatures. For the gas temperature, since rotational equilibrium is likely for many conditions of interest, measurement of the relative intensities of rotational lines will in principle yield a rotational temperature which often can safely be assumed equal to the gas translational temperature. However, if this is done by conventional emission spectroscopy the usual Abel inversion of multiple lines can lead to unreliable results. A promising alternative is the measurement of rotational temperature (as well as species concentration) using laser-induced fluorescence. However, these laser-based point measurements are notably difficult to perform in a luminous plasma, as evidenced by the scarcity of reported verified results. The scattering measurements of line width reported by Snyder and Reynolds[9] are a notable exception. Another possibility for the measurement of the gas temperature is the use of wavelength tunable diode lasers to obtain Doppler line widths. Because of the weak temperature dependence and occurrence of other forms of broadening this measurement must be performed with unusual precision to provide useful results.[10]

3.2 More Complex Plasmas

Departures from equilibrium in the population of free-electrons in recombining thermal plasmas are normally attributed to finite rates for three-body electron recombination. Indeed, in atomic or fully dissociated molecular plasmas electrons recombine via reactions of the type $X^+ + e + M \rightleftharpoons X + M$ (where $X = N$ or O , and M is a third-body electron or heavy particle) which are relatively slow as they involve ternary collisions. If molecular ions are present in the plasma, electrons can recombine instead via the dissociative recombination reactions $XY^+ + e \rightleftharpoons X + Y$. The latter reactions are typically much faster and equilibrate more rapidly than three-body electron recombination reactions. Likewise, charge exchange reactions are generally fast as well. As a result, the preferential channel for electron recombination in molecular plasmas is via dissociative recombination, and the degree of ionizational nonequilibrium is ultimately determined by the rates of (three-body) atom recombination reactions:



Since these reactions are generally slow, we have the surprising result[11] that ionizational nonequilibrium in air plasmas is caused by finite-rate neutral chemistry. Reliable rates for atom recombination reactions are therefore required to correctly predict the extent of ionizational nonequilibrium. Unfortunately, many of these rates are not known with good accuracy, in particular at temperatures below 7000 K.[7]

In our laboratory, experiments have been conducted to assess the various rates proposed in the literature.[12-14] To this end, electron recombination was measured as a function of residence time in recombining plasmas flowing through water-cooled, 1 cm diameter brass test-sections mounted on the exit nozzle of the torch as shown in Fig. 2.1. As discussed below, three types of plasmas (air, nitrogen/argon, and air/argon) were investigated, each yielding an assessment of the rates of reactions 1 and 2 above.

3.2.1 Air Plasma Experiments

An air plasma flow, initially in equilibrium at a temperature of 7,160 K at the nozzle exit, was cooled to ~4,900 K within ~400 μs over a distance of 25 cm. Temperature, electron number density, and line-of-sight spectral emission measurements were made at the exit of test-sections with lengths between 10 and 25 cm in 5 cm increments in order to examine plasma recombination as a function of residence time. Radial temperature profiles were obtained by Abel-inverting lateral profiles of the absolute intensity of the atomic oxygen triplet at 777.4 nm, and electron number densities were measured from the Stark broadening of the H_β line at 486.2 nm (to this end, a small quantity of ~1 slpm of H₂ was premixed with 100 slpm of air before injection into the torch).

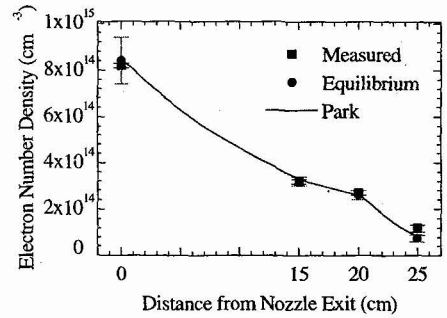


Figure 3.3 Measured and predicted electron number densities in air at 0, 15, 20, and 25 cm.

As can be seen in Fig. 3.3, the measured electron number densities were found to be close to their equilibrium values. Furthermore, the emission spectra were compared with equilibrium simulations performed with the accurate radiation code NEQAIR2[15, 16] recently developed by our group as an extension to the NASA code NEQAIR.[17] Differences between the measurements and LTE simulations would be indicative of nonequilibrium conditions in the experiment.[18] At all locations, however, the equilibrium radiation calculations reproduced all measured spectral features originating from the B state of N₂⁺, the B and C states of N₂, the A, B, and C states of NO and the B state of O₂ within experimental and modeling uncertainties. Thus the plasma remains close to equilibrium throughout the reaction zone.

These experimental observations were used to assess the reaction mechanisms proposed by Dunn and Kang,[12] Gupta et al.,[13] and Park.[14] To this end, the dynamic evolution of species concentrations along the axis of the plasma flow was modeled using the chemical kinetics solver CHEMKIN[19] and the three sets of ~30 reactions and rates.[12-14] Figure 3.4 shows the predicted nonequilibrium concentration factors, defined as the ratio of predicted to equilibrium mole fractions. Thus a value of unity indicates equilibrium, and a value greater than 1 indicates an overpopulation of the given species. Figure 3.4 also illustrates the rather poor understanding of the controlling rates of ionizational nonequilibrium, and the resulting uncertainty in the predicted electron concentration. As can be seen in Fig. 3.4, the mechanism of Park predicts that the air plasma remains close to equilibrium throughout the reaction zone, in agreement with our experimental observations, whereas the mechanisms of Dunn and Kang, and Gupta et al. predict departures from equilibrium in the electron number density by up to a factor 3 at the exit of the 25 cm test-section. Since overall plasma recombination, and in

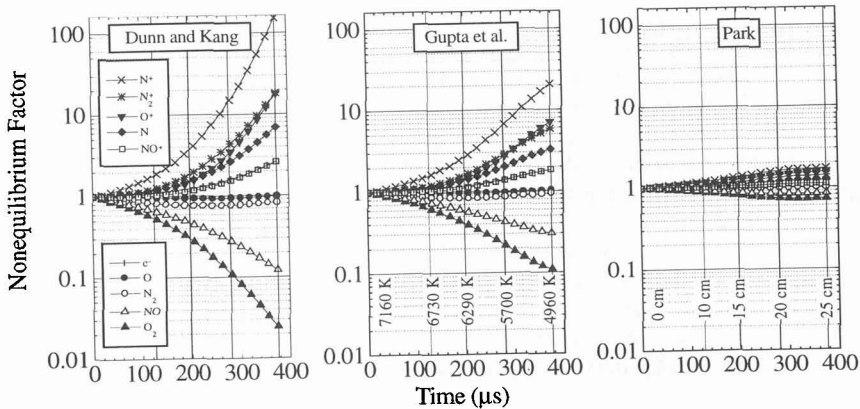


Figure 3.4 Nonequilibrium factors predicted by three reaction mechanisms for the recombining air plasma.

particular electron recombination, is mainly controlled by the rate of Reaction 1 under these conditions, it appears that the rate of Reaction 1 should be at least as fast as the rate proposed by Park.[14]

3.2.2. Nitrogen/argon plasma

To assess the rate of $N + N + M \rightleftharpoons N_2 + M$ (Reaction 2), separate experiments were conducted with a nitrogen plasma (100 slpm N_2), premixed before injection into the torch with 50 slpm of argon to provide stable operating conditions, and 2.3 slpm of H_2 for electron density measurements. The plasma recombined over a length of 15 cm and within 250 μs from 7200 to 4700 K. Measurements were made at the 0, 10 and 15 cm locations. Temperature profiles were obtained from the Abel-inverted intensities of lines of argon (763.5 nm) and hydrogen (H_α and H_β), and of the band head of the N_2^+ (B-X) transition. As shown in Fig. 3.5, electron number densities at 0 and 10 cm were found to be close to equilibrium. In contrast, at 15 cm an electron overpopulation factor of 135 ± 60 was observed, consistent with (although higher than) the value of 45 predicted with Park's mechanism (see Fig. 3.5). Since here electron recombination is controlled by the rate of Reaction 2, we concluded that the rate proposed by Park for that reaction is accurate to within approximately a factor three over the considered temperature range. Further work is in progress[20] using a quantitative coupled flow-chemistry model to provide a definite assessment and, if necessary, a corrected value for this rate.

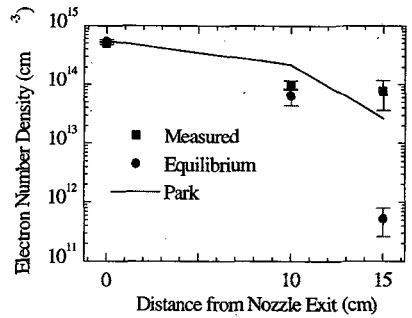


Figure 3.5 Electron number densities in the nitrogen/ argon plasma.

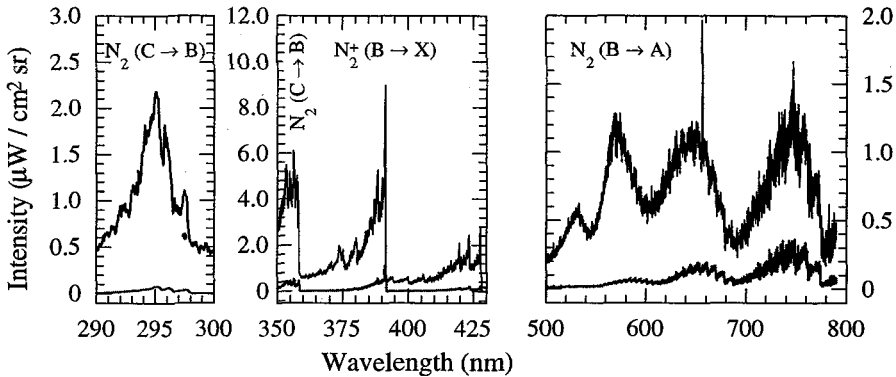


Figure 3.6 Nitrogen/argon plasma at 15 cm downstream of nozzle exit: Measured spectrum (black) and computed LTE spectrum (grey).

We obtained experimental confirmation of the slow recombination of N atoms from spectral emission measurements at 15 cm where the excess free electrons appears conjointly with a significant enhancement of the populations of the B and C states of N_2 . This can be seen in Fig. 3.6 wherein the measured spectrum appears much more intense than the computed equilibrium spectrum, unlike the case at 0 and 10 cm where the two spectra agree to within better than 10%.⁹ For the B state of N_2 , the observed difference indicates large departures from a Boltzmann distribution in the vibrational levels. The measured vibrational overpopulation distribution (Fig. 3.7) is characteristic of the Lewis-Rayleigh afterglow mechanism[21] by which N atoms recombine preferentially into levels 10-12 of the B state of N_2 and thus produce the observed vibrational distribution when an excess of N atoms exists. Similarly,

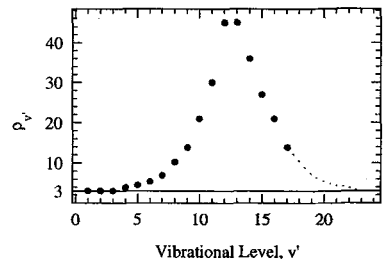


Figure 3.7 Measured vibrational overpopulation in the N_2 B state.

the populations of the N_2 C state vibrational levels are partially coupled to the population of N atoms as a result of fast inverse predissociation.[18] The overpopulation factors for these levels, measured to be approximately 32, therefore confirm the presence of N overpopulation.

The foregoing observations clearly show that under nonequilibrium conditions great care must be exercised when interpreting both temperatures and concentration measurements.

3.2.3. Air/argon experiments

To provide a better assessment of the rate of Reaction 1 (on which the pure air studies permitted us to place a lower limit), experiments were conducted with a ~10% air - 90 % argon plasma cooled from 7,900 K to approximately 2,700 K over a time of ~1.3 ms and a distance of 65 cm. Dilution of ~10% air in argon causes the recombination of nitrogen atoms to be about one order of magnitude slower than in the pure air plasma case as the third body efficiency of argon in Reaction 1 is approximately 20 times smaller than the third body efficiencies of N and O atoms. By slowing the overall N atom recombination, it should be possible to observe significant chemical and ionizational nonequilibrium, and thus to place an upper limit on the rate of Reaction 1. Even at this relatively high dilution level, the electron recombination path remains the same as in pure air because electrons still recombine preferentially via the dissociative recombination reaction $NO^+ + e \rightarrow N + O$, even though NO^+ is no longer the dominant ion here.

Experiments were conducted with 15.6 slpm of air premixed with 162 slpm of argon and a small quantity (2.3 slpm) of H_2 for electron number density determinations. Optical emission was collected at the end of test sections ranging from 0 cm (nozzle exit) to 65 cm in length. Because the temperature varies from ~8000 K at the nozzle exit to ~2500 K at the 65 cm test section exit, various techniques were employed to obtain temperatures and electron number densities. At 0, 10, and 15 cm, temperature profiles were obtained from the Abel-inverted line intensities of oxygen (777.3 nm), argon (763.5 nm) and hydrogen (H_α). At each location, the temperatures determined from the three atomic lines were found to agree within 150 K. At 40, 50, and 65 cm, the excited state populations of atomic species could not be seen in emission, but the temperatures could still be accurately measured from the temperature sensitive shape of the measured OH $A^2\Sigma^+ \rightarrow X^2\Pi_i$ band. This was done by comparing numerical OH spectra[22] at various temperatures normalized to the 309.2 nm peak to the measured line of sight spectra. This shape-matching technique yields centerline temperatures with an accuracy of ~200 K. The remainder of the temperature profile was obtained from the Abel-inverted intensity of the 306.8 nm peak relative to the 304 nm baseline. More details can be found in Ref.[23].

The overpopulation factors shown in Fig. 3.8 were computed with CHEMKIN using the rates of Park[14] for air and appropriate rates for reactions with argon and hydrogen.[18] In Fig. 3.9, the measured electron number densities are compared with those predicted using Park's mechanism. At 0, 10, and 15 cm, direct measurements of n_e were made via the Stark broadening of the H_β line at 486.1 nm. Error bars on these data points (Fig. 3.9) reflect uncertainties on measured electron number densities and on centerline temperatures. At the exit of longer test-sections, the intensity of the H_β line was very weak and therefore no direct measurements of electron number densities could be made. However, as discussed in Ref.[23], the electron number density at these locations could be determined from the measured overpopulation factors of the C state of NO.

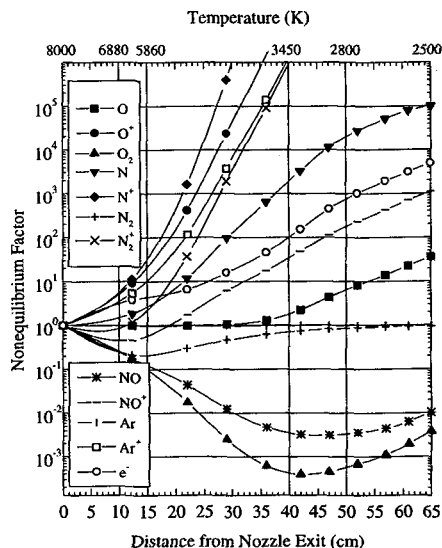


Figure 3.8 Predicted nonequilibrium factors for the recombining air/argon plasma (Park's mechanism).

Since the three body recombination of NO accounts for about 38 to 20 % of the total N atom consumption between 15 and 60 cm downstream of the nozzle exit (the balance being due to the Zeldovich reactions whose rates can be considered well known), the rate of $N + O + M \leftrightarrow NO + M$ may be too slow. While Park concludes that this rate is known within a factor three,[7] examination of his compilation of relevant NO thermal dissociation rate measurements seem to warrant a factor ten uncertainty on this rate. As discussed in Ref.[23], multiplying the third body efficiencies in Reaction 1 by a factor 10 improves the agreement between measurements and predictions for test-sections ≤ 45 cm, but produces a recombination rate that is too fast at longer distances. Several issues must be examined in order to draw more definite conclusions about these third body efficiencies. First, a detailed collisional-radiative model is warranted to better determine the degree of coupling between the NO C state and N and O atoms. And second, possible departures from a Maxwellian distribution for the free-electrons and their consequences on rate coefficients must be considered. A preliminary analysis of these effects indicates that departures from a Maxwellian distribution may occur at locations > 35 cm.[23] These various issues are currently being examined in order to provide a better assessment of the rate of NO three-body recombination.

3.3 Diagnostics of Diamond Synthesis Environments

Over the past several years, we have investigated the nonequilibrium synthesis of diamond thin films in several high and low pressure facilities. Although the diamond synthesis environment is quite challenging to investigate due to its highly nonequilibrium neutral and plasma chemistry, it is also within reach of state-of-the-art numerical simulations based on relatively well established systems research. We have made extensive use of laser-based diagnostics and comparisons with sophisticated models to learn about the process of diamond Chemical Vapor Deposition (CVD).

3.3.1 Degenerate Four-Wave Mixing (DFWM)

It is quite difficult, for many diagnostic techniques, to provide useful and accurate information in the harsh and nonequilibrium environment of atmospheric pressure PACVD of diamond thin films. Sensitive measurement of temperature and trace radical concentrations within a reacting boundary layer is a challenging problem due to the highly luminous environment, small spatial scales, and steep thermal and concentration gradients. It is in this environment where the application of sensitive, laser based diagnostic techniques can allow the detailed measurement of temperature and trace radical concentrations to be made, and compared to models of the deposition environment. The application of a powerful non-linear laser spectroscopy, degenerate four wave mixing (DFWM), as a gas-phase optical diagnostic has opened the door for significant advancement in the area of atmospheric pressure plasma chemistry, since it can provide high sensitivity and spatial resolution with a coherent, phase conjugate signal which can be readily discriminated against the plasma.[24-27]

The DFWM technique[28] utilizes three laser beams of a single wavelength interacting with the plasma to produce a fourth spatially coherent, polarized signal beam that can be collected with high efficiency, and effectively filtered from the intense plasma luminosity. This feature is perhaps the greatest advantage of DFWM over other traditional diagnostic tools of atmospheric pressure plasmas which are often disabled or corrupted by the intense background luminosity. In thermal plasma CVD, we find DFWM to be an extremely useful nonintrusive probe of the plasma, capable of providing high spectral and spatial resolution, and permitting measurements of temperature and relative species concentrations of trace radicals under conditions in which other spectroscopic techniques fail. Since DFWM can be used to probe the ground state of electronic transitions, it is much less subject to

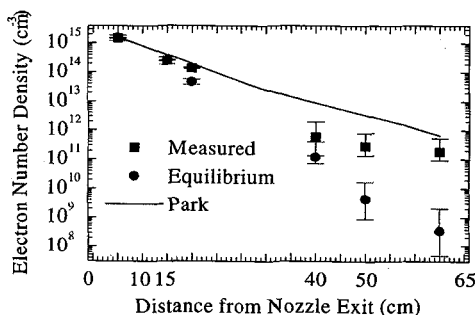


Figure 3.9 Electron number densities in the air/argon plasma.

misinterpretation as a result of nonequilibrium effects[29] than conventional techniques such as optical emission spectroscopy (OES).

In a program to investigate the thermal plasma diamond CVD environment, experiments were conducted using the RF plasma torch facility, inside a water cooled quartz test section which is shown in schematic cut-away along with the plasma torch head in Figure 3.10. Open-ended laser access ports, approximately 6.5 cm downstream of the nozzle exit, enable the DFWM pump and probe beams to enter and exit the reactor unhindered, and to cross at a location directly below the stagnation point of a diamond growth substrate. Substrates are supported within the quartz test section in a stagnation point flow geometry by means of a water cooled holder. The substrate can be vertically translated in-situ to allow laser measurements to be made at various points through the boundary layer. Substrate temperature is monitored with a Minolta/Land Cyclops 152 infra-red optical pyrometer. Reactant gases (hydrogen and methane) are premixed with the carrier gas (argon) before passage through the RF discharge.

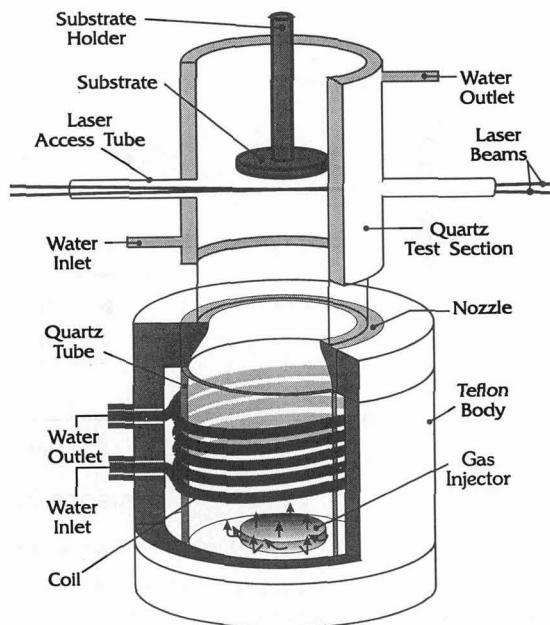


Figure 3.10 Schematic of RF-ICP reactor.

In these studies, DFWM was used to perform in-situ measurements of the trace radical CH to determine vibrational temperatures, rotational temperatures, and relative species concentration measurements (including profiles of these quantities through the reacting boundary layer above the growth substrate), and compared to results of a detailed one-dimensional model[30] of the deposition environment. It was desired to make in-situ measurements during normal operation of the atmospheric pressure RF-ICP diamond synthesis reactor - with a substrate in place, and growing diamond. The conditions chosen for these studies were indeed diamond growth conditions (although they were not optimized for best possible growth) and all measurements reported here were taken with the growing substrate in place. The reactor gas feed mixture was comprised of 106.5 l/min Ar, 12.0 l/min H₂, and 0.8% to 10% CH₄ (in H₂) premixed before introduction to the plasma torch. Calorimetric energy balance of the reactor indicates a net plasma enthalpy of 6 kW leaving the nozzle exit. The molybdenum substrate had a measured surface temperature of 1035°C.

The CH radical was probed with in-situ DFWM measurements of the CH $A^2\Delta \leftarrow X^2\Pi(0,0)$ system near 431 nm. A comparison of measured CH vibrational and rotational temperatures along the stagnation line of the substrate with values from the computational simulation is shown in Figure 3.11. Boundary conditions for the simulation are the measured freestream temperature of 3900 K, an estimated freestream velocity of 8 m/s, and the measured substrate temperature of 1035°C. We can see in Figure 6 the predicted thermal boundary layer (≈ 6 mm thick) with a steep fall off in temperature very close to the substrate. The measured CH vibrational temperatures are in close agreement with the predictions, although the loss in signal of the $v=1$ transitions in the cooler region very near the substrate prevents accurate vibrational temperature measurement for distances < 2 mm. Rotational temperature measurements from the CH $v=0$ lines, which remain strong enough for accurate measurement closer to the substrate are in good agreement with both the measured vibrational temperatures and the computational simulation. It is possible to make rotational temperature measurements even closer to the substrate than shown in Figure 3.11, but for these experimental conditions the CH concentration in that region has dropped below approximately 2 ppm, which is our current detection limit.

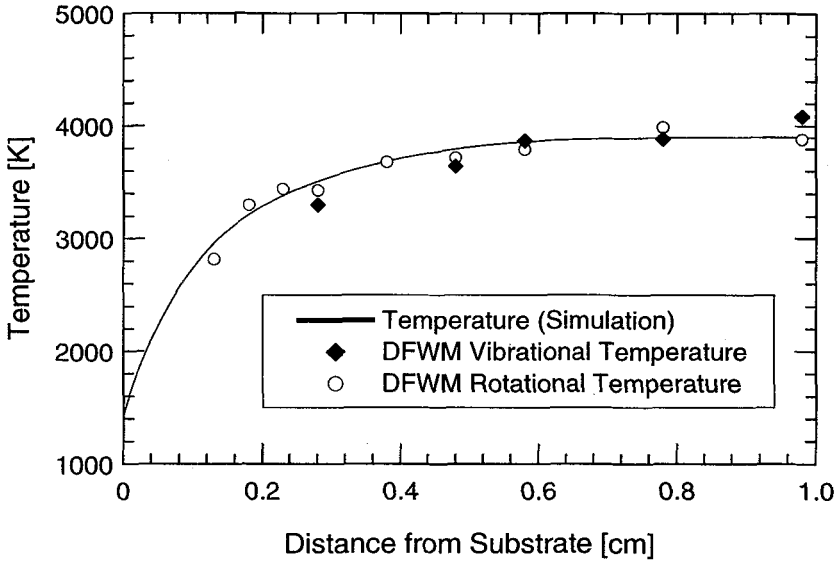


Figure 3.11 Boundary layer temperature profiles.

Measurements of the relative CH mole fraction within the substrate boundary layer are compared to results of the computational simulation in Figure 3.12. The CH mole fraction is approximately 30 ppm in the freestream (3900 K) and is predicted to first rise within the approximately 6 mm thick boundary layer (due to production) as the plasma cools toward approximately 3700 K, reaching a peak of approximately 52 ppm at 2.5 mm from the substrate surface, then to be destroyed as the plasma cools further on its approach to the substrate surface.

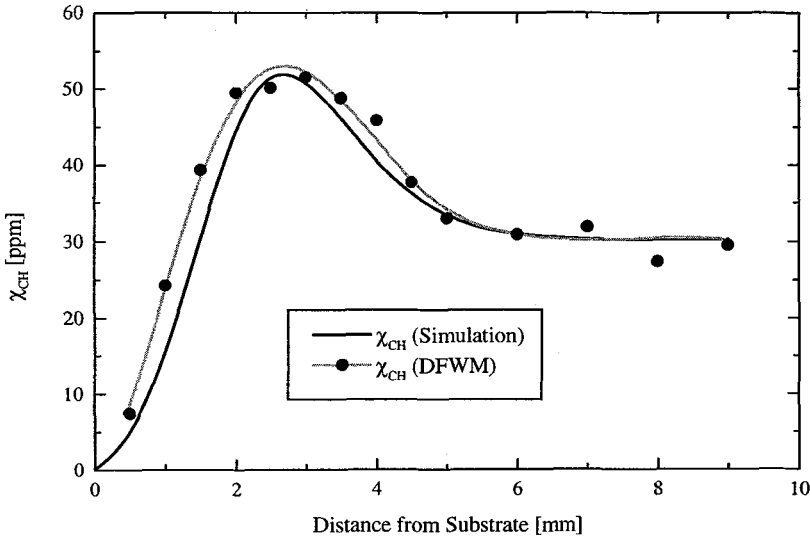


Figure 3.12 CH concentration profile.

A more direct insight into the boundary layer chemistry can be gained by comparing the CH mole fraction throughout the boundary layer to its equilibrium value at the measured local temperature. This is displayed in Figure 3.13a where we can observe the CH to remain near its equilibrium values until approximately 2 mm from the substrate surface where it then rises to approximately 1000 times the

equilibrium value close to the surface. The measured nonequilibrium is in close agreement with the predicted values. By studying the numerical simulation, we find that this nonequilibrium observed in the CH mole fraction is in fact driven by the atomic hydrogen chemistry. The timescale of transit through the boundary layer is insufficient for the atomic hydrogen recombination mechanisms to maintain atomic hydrogen concentration in equilibrium with the local gas temperature. The calculated atomic hydrogen nonequilibrium is shown in Figure 3.13b. The fast reactions between atomic hydrogen and the CH_x hydrocarbons maintains a partial equilibrium amongst these species, and thus an overpopulation of atomic hydrogen maintains an overpopulation of all CH_x hydrocarbons (notably CH_3 , thought to be the major growth precursor). The interrogation of this environment using DFWM has thus allowed us to see that the nonequilibrium behavior of atomic hydrogen chemistry is a critical component to the atmospheric pressure synthesis of diamond thin films.

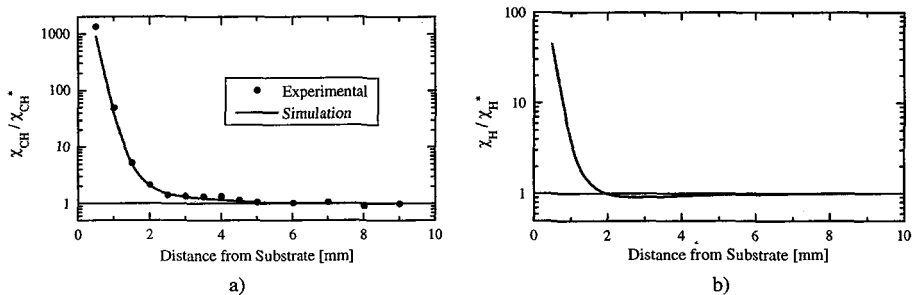


Figure 3.13 a) CH nonequilibrium profile, b) atomic hydrogen nonequilibrium profile.

3.3.2 Cavity Ring-Down Spectroscopy (CRDS)

The methyl radical has fundamental importance for studies of diamond film growth by chemical vapor deposition (CVD) because it is regarded as a gas-phase precursor of the diamond film.[31-33] Therefore, starting with the first report in 1988[34] on infrared detection of CH_3 during filament-assisted growth of diamond, several techniques has been applied to monitor methyl radicals in a CVD reactor, including REMPI spectroscopy [35-39], UV absorption spectroscopy [40, 41], and mass spectrometry [42]. These techniques, however, can be intrusive (as in the case of REMPI) and of limited spatial resolution (mass spectrometry) and sensitivity (absorption). The CH_3 mole fraction in a CVD reactor has been also modeled,[43] and the relation between the model predictions and growth rate and film quality has been studied.[44, 45]

We have developed diagnostics for the methyl radical based on the cavity ring-down technique (CRDS).[46-50] CRDS is a highly sensitive absorption spectroscopy that determines the absolute absorbance of a laser pulse passing through a sample. In a manner similar to single-pass laser absorption spectroscopy, this measurement is performed with two-dimensional spatial resolution; however, unlike the case of single-pass absorption spectroscopy, CRDS measures absorbance as low as 10^{-5} - 10^{-7} and is insensitive to shot-to-shot power fluctuations in the laser pulses. These features make CRDS suitable for high sensitivity measurements.

The hot-filament reactor (shown in Figure 2.3) consists of a 5-way stainless steel cross 4 inches in diameter. A two-stage mechanical pump (E2M40, Edwards) is used to evacuate the chamber to the minimum pressure of 4×10^{-3} Torr. The chamber is filled with 20 Torr mixture of H_2 with 0.5 % of CH_4 flowing at a rate of 100 sccm. The tungsten filament is 20 mm long and 200 μm in diameter. It is positioned horizontally inside the chamber using two tungsten posts, 4 cm long and 1.5 mm in diameter, mounted on water-cooled copper electrodes. The filament is resistively heated with dc current to a brightness temperature of 2300 K, which is monitored with a disappearance pyrometer (Pyro Micro-Optical Pyrometer). The substrate is made of a molybdenum strip (4 mm x 20 mm x 250 μm) and is resistively heated. The substrate temperature is monitored with a K Type thermocouple which is welded to the rear surface. The front surface is scratched with 10 μm diamond paste. The reactor condition is stabilized for more than 12 hours before CRDS measurement. In these studies, the ring-down cavity is

62 cm long with mirrors mounted in 1.5 inch thick aluminum blocks separated with four stainless steel rods 3/4 inch in diameter for cavity stability. The reactor is placed inside this cavity frame and connected to the mirror mounts by means of flexible bellows. A laser pulse injected into the cavity circulates back and forth along the same path between the cavity mirrors, crossing the reactor parallel to the filament and substrate. The distance between the filament and the pulse path is controlled with a micrometer that moves the reactor on a translation stage.

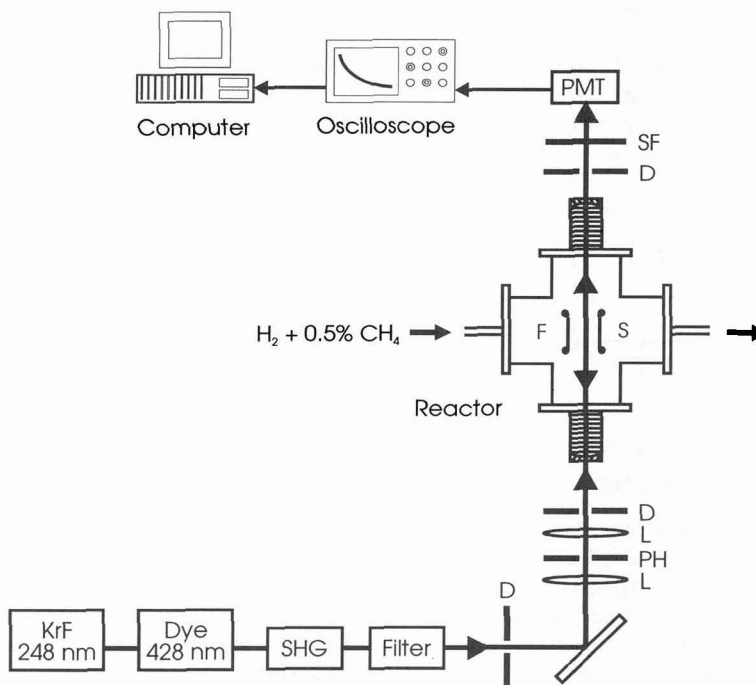


Figure 3.14 Schematic of the CRDS system / hot-filament reactor. D = iris diaphragm, L = lens, PH = 50 μm pinhole, SF = spectral filter, F = Filament, and S = substrate.

determined directly by the ring-down time τ_0 of the empty cavity. The TEM_{00} cavity mode has approximately a cylindrical form with a waist of 0.5 mm in diameter.

The light transmitted through the back mirror of the cavity was collected by a photomultiplier (PMT) and the PMT signal as a function of time was recorded on an HP 54510A digitizing oscilloscope with 2 ns temporal resolution. The ring-down waveforms digitized on the oscilloscope were transferred to a PC computer, averaged, and the ring-down time τ was obtained from a real-time computer fit. The CH_3 absorbance is then obtained from the measured τ and τ_0 via the relation $\alpha l_s = t_r/2(1/\tau - 1/\tau_0)$, where t_r is the cavity round-trip time, and l_s is the sample length.

Figure 3.15 shows spatial profiles of the CH_3 number density (absorbance) within the hot-filament reactor at two different substrate temperatures. The filament temperature is held constant at 2300 K, the total pressure is 20 Torr, and the gas mixture is 0.5% CH_4 in H_2 flowing from left to right at a flowrate of 100 sccm. One can observe that the concentration of methyl radicals falls rapidly with increasing distance from the filament, and that the methyl radical concentration increases significantly at the higher substrate temperature. It is interesting to note that the methyl concentration well upstream of the filament is strongly influenced by the substrate temperature, possibly due to an overall increase in the reactor temperature field and hence methyl radical production. One can also observe that for the 900 $^\circ\text{C}$ substrate condition that the peak methyl concentration occurs at a distance away from the filament (approx. 2 mm). This peaked result agrees qualitatively with the behavior of the CH_3 REMPI signal as a function of a distance from the filament reported by Ota and Fujimori,[39] but the peak CH_3

The schematic of our CRDS setup is shown in Figure 3.14. An excimer-laser-pumped dye laser (Lambda-Physik) working with Coumarin 440 was used as the pulse source. The pulses were 15 ns long with 0.18 cm linewidth. After frequency doubling in a BBO crystal with an Inrad Autotracker, the 214 nm pulse was shaped with the system of pinholes and lenses to match approximately the TEM_{00} transverse mode of the optical cavity. The quasi-hemispherical optical cavity was 62 cm long with a flat entrance mirror and a 2 m curvature concave back mirror. The mirrors were coated by Lightning Optical Corp. and achieved 98.9 % reflectivity at 213.9 nm, as determined directly by the ring-down time τ_0 of the empty cavity. The TEM_{00} cavity mode has approximately a cylindrical form with a waist of 0.5 mm in diameter.

concentration we find is two orders of magnitude higher than their estimate. Goodwin, Glumac, and Corat[38] also measured spatial profiles of the CH_3 REMPI signal in the hot-filament reactor; however, their data do not extend to positions close to the filament and cannot be directly compared with our observations.

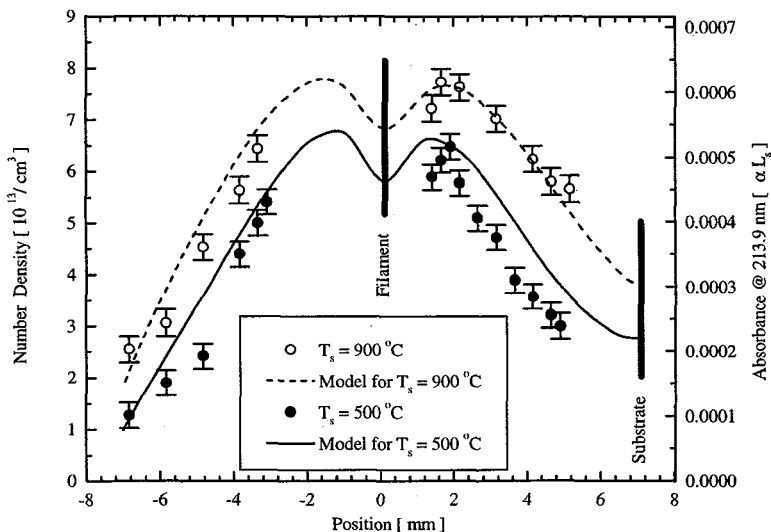


Figure 3.15 Spatial profiles of the measured CH_3 number density (absorbance) within the hot-filament reactor at two different substrate temperatures along with the model predictions of Mankelevich. The filament temperature is 2300 K, the total pressure is 20 Torr, and the gas mixture is 0.5% CH_4 in H_2 flowing from left to right at a flowrate of 100 sccm.

Figure 3.15 also shows the methyl radical concentration profile predicted by the two-dimensional model of Mankelevich et al.[51, 52] for the same reactor conditions probed experimentally. In this two-dimensional model conservation equations for species, mass, momentum, and energy are solved including molecular and thermal diffusion, along with chemistry for 15 species via 38 reversible reactions. Temperature “slips” at the filament and substrate surface are prescribed from a separate Monte Carlo simulation. The largest uncertainty in this model is the production rate of atomic hydrogen at the filament surface. The results of the model prediction are in good agreement with the experimental measurements both in shape and relative magnitude for the two cases presented. Deviation of the model and experimental data near the substrate in the case of $T_{\text{sub}}=500\text{ °C}$ is most likely due to the sensitivity of methyl radical production to the local gas temperature.

Methyl radical number density measurements were also taken very near the substrate surface (within ~ 0.5 mm) as a function of both substrate and filament temperature. Results of those measurements are shown in Figures 3.16 and 3.17 respectively. In both cases the reactor pressure was 20 Torr with a mixture of 0.5% CH_4 in H_2 flowing at a rate of 100 sccm, and the substrate prepared by operating at diamond growth conditions of $T_f = 2300\text{ K}$, $T_s = 900\text{ °C}$ for approximately 12 hours. In Figure 3.16, the filament temperature was held at 2300 K while the substrate temperature was increased from 600 °C to 1200 °C. The power to the substrate was increased after each data point by increments of approximately 50 °C and allowed to stabilize for 10 minutes before the next point was taken. One can see an approximately linear increase in the near surface methyl radical concentration with increasing substrate temperature. This is in qualitative agreement with the results of Corat and Goodwin[37] for the near surface region, although our data does not extend to high enough temperature to confirm their observed high temperature roll-off in methyl concentration. Our observed activation energy of the near surface radical concentration, based on substrate temperature, is 4.2 ± 0.2 kcal/mol. This value agrees with the value reported by Corat and Goodwin.[37]

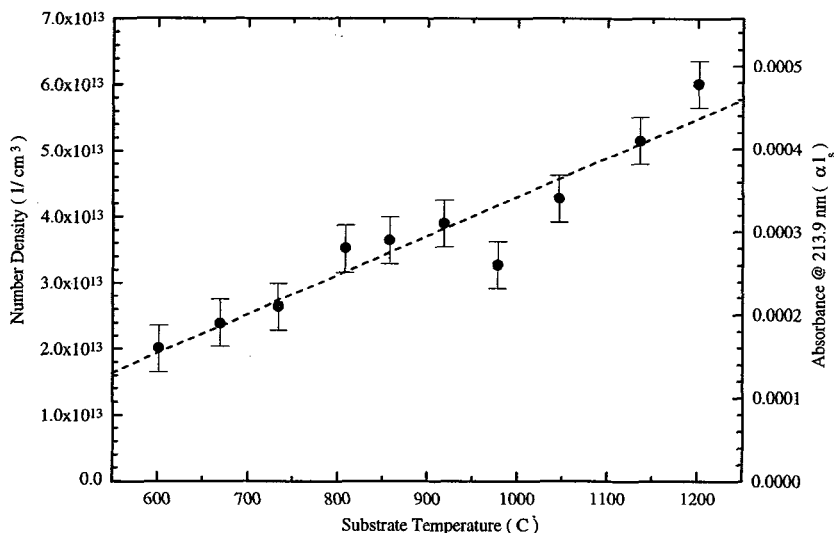


Figure 3.16 Variation of the CH_3 number density (absorbance) near the substrate surface (within ~ 0.5 mm) as a function of substrate temperature. The filament temperature is 2300 K, the reactor pressure is 20 Torr, and the gas mixture is 0.5% CH_4 in H_2 with a flowrate of 100 sccm.

In Figure 3.17, the substrate temperature was held at 900 °C while the filament temperature was increased from approximately 2000 K to approximately 2550 K. We observe the near surface methyl concentration to first increase strongly with increasing filament temperature, and then to saturate somewhat above 2400 K. This strong increase is in qualitative agreement with the REMPI measurements of Corat and Goodwin,[37] but we do not observe a decrease in methyl concentration above 2300 K as evident in their measurements. Our data trends do, however, compare favorably to the model predictions of Kondoh et al.[44]

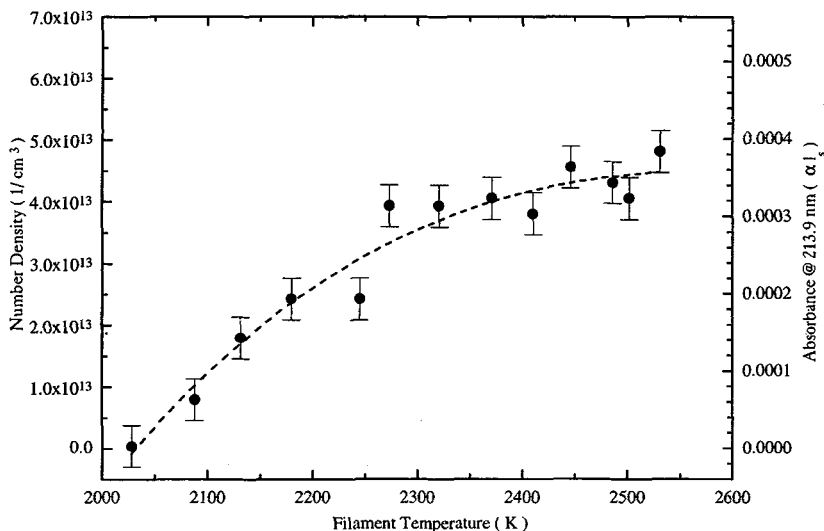


Figure 3.17 Variation of the CH_3 number density (absorbance) near the substrate surface (within ~ 0.5 mm) as a function of filament temperature. The substrate temperature is 900°C, the reactor pressure is 20 Torr, and the gas mixture is 0.5% CH_4 in H_2 with a flowrate of 100 sccm.

On the basis of our observations we conclude that the CRDS technique can be used for quantitative diagnostic of methyl radicals with high sensitivity. We have applied CRDS to the measurement of methyl radicals generated in a hot-filament reactor. We have observed a strong sensitivity of the methyl radical concentration throughout the reactor to the substrate temperature. At some operating conditions, we also observe the methyl radical concentration to peak at the location several mm from the filament surface. This behavior of CH_3 with distance from filament is not predicted by current one-dimensional models of the reactor. This off-filament maximum concentration indicates that the methyl is not generated at the filament surface, but rather by gas-phase reactions. The near surface concentration of methyl is observed to increase linearly with increasing substrate temperature, and is found to increase and saturate with increasing filament temperature.

3.3.3 Two-photon Atomic Laser Induced Fluorescence (TALIF)

Atomic hydrogen plays an important role in the diamond synthesis environment by affecting both the quality and quantity of diamond films produced. With this in mind, the need to nonintrusively detect and monitor ground state atomic hydrogen, and probe its role in nonequilibrium chemistry becomes quite clear. Unfortunately, due to the large energy spacing between the ground state of atomic hydrogen and its first excited state (10.2 eV), single photon optical techniques would require wavelengths of 121.5 nm in the vacuum ultraviolet. This wavelength is strongly absorbed by most materials, and only propagates easily through vacuum. These drawbacks have led to the application of two photon laser based techniques such as two photon atomic laser induced fluorescence (TALIF).

The TALIF technique uses two photons of laser light to promote a ground state atom to one of its excited states, and monitors the resultant fluorescence (either to another excited state or to the ground state). In this manner, a laser of longer wavelength (243nm for the Lyman α transition) can be utilized, and is much easier to produce and propagate. We have carried out preliminary experiments to develop and use a TALIF technique to detect ground state atomic hydrogen in a hot-filament reactor. The TALIF technique we are using is shown schematically in Figure 3.18 below. In this technique, a ground state atomic hydrogen atom absorbs two photons from a 243 nm laser field, and is promoted from the 1S state to the 2S state. The 2S state is collisionally coupled to the nearly iso-energy 2P state and the two states rapidly equilibrate. The subsequent fluorescence from the 2P state to the 1S state (Lyman α at 121.5 nm) is then be detected with a solar blind PMT whose photocathode is placed within the hot filament reactor. A sample spectra taken within the hot filament reactor is shown below in Figure 3.19. In this case, the reactor was filled with 20 Torr of H_2 , and the spectra was measured 4.5 mm from the filament surface.

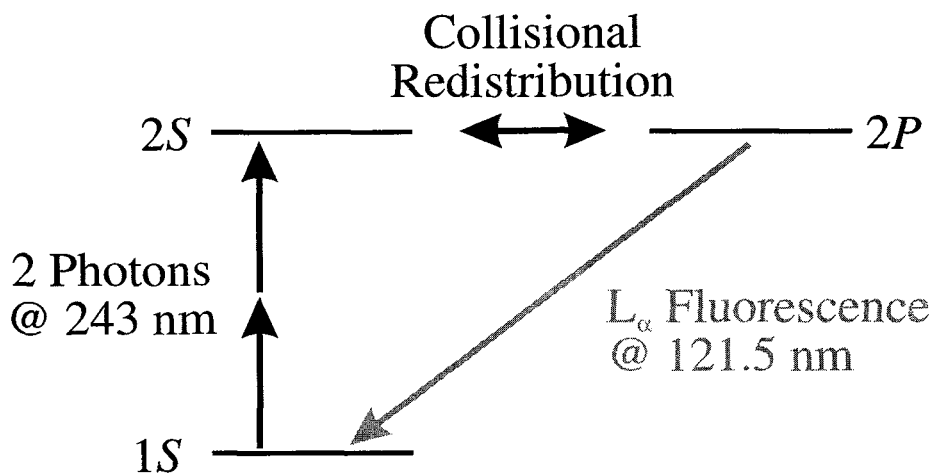


Figure 3.18 Schematic of the TALIF technique for atomic hydrogen detection.

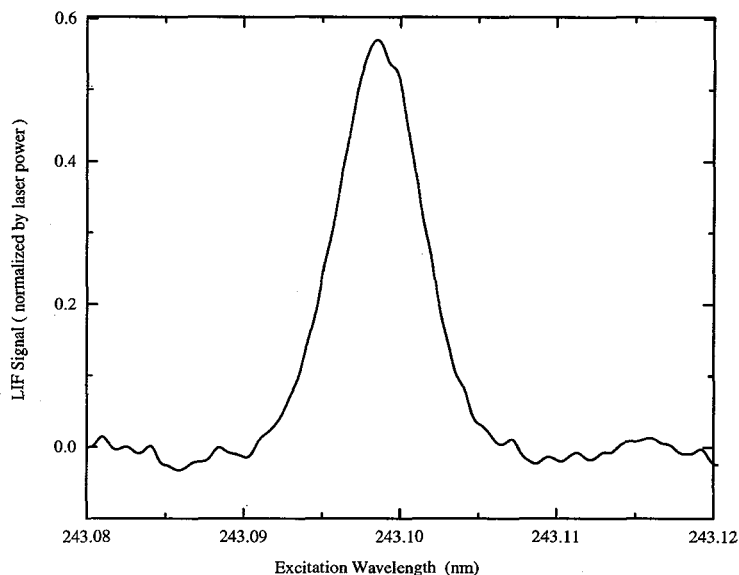


Figure 3.19 TALIF spectra of atomic hydrogen in a hot filament reactor.

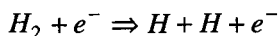
Using this TALIF technique, we are developing methods to determine both the concentration and temperature of ground state atomic hydrogen with the hot filament reactor. These measurements, in conjunction with CRDS measurements of the CH_3 radical will yield an important database of experimental measurements to which models of the deposition environment may be compared.

3.4 Discharge Induced Nonequilibrium Plasma Chemistry

Several radical species in the diamond growth environment are thought to contribute to the deposition of the diamond thin-films. Of these, atomic hydrogen is believed to be particularly important.[53-55] Atomic hydrogen makes surface sites available to carbon containing species needed for the diamond growth process by abstraction of surface hydrogen. Atomic hydrogen also acts to incorporate adsorbed hydrocarbon radicals into the diamond lattice. Carbon containing radical fluxes factor directly into the diamond growth rate, as they are the source of carbon for continued diamond growth,[55] and are often strongly linked to the available atomic hydrogen concentration.

There are several ways to increase the radical concentration at the growth surface, leading to rapid growth of high-quality diamond. It has been shown[56, 57] that by increasing the plasma velocity, the boundary layer thickness above the deposition surface is thinned. This effect decreases the time available for recombination of radical species that are created in the freestream and the boundary layer as they approach the substrate. This can lead to higher fluxes of these species to the growth surface and higher growth rates of CVD diamond. A factor of 5 increase in growth rate has been observed when the plasma velocity was increased by an order of magnitude.[56] Additionally, recent analysis of scaling relations for convection-dominated reactors has found that the use of high pressure (≥ 1 atm), sonic flow conditions will maximize the H atom concentration delivered to the deposition surface.[53, 54] A different approach to increase radical fluxes to the deposition surface involves actively driving the boundary layer chemistry to a greater degree of nonequilibrium by means of discharge induced plasma chemistry.[58-60] Matsumoto, et al. [60, 61] applied a positive potential to the deposition surface in a sub-atmospheric dc arcjet and found a twofold increase in diamond growth rate as compared with an unbiased case, although the deposited films had a low degree of uniformity across the deposition surface. They implied that an enhancement in gas phase dissociation near the substrate was the cause for the increased deposition rate.[61] Conversely, negative-biasing of the substrate has been used in low pressure, microwave reactors to enhance and control the nucleation of CVD diamond.[62, 63]

We have conducted preliminary experiments to address the secondary discharge method as a means of augmenting the deposition rate while maintaining a high degree of film quality. By biasing the deposition surface with respect to the plasma, the free electrons gain kinetic energy from the imposed electric field. These energetic electrons can promote super-equilibrium concentrations of radical species in the boundary layer via bond-breaking collisions with the molecular species. In particular these electrons can shift the balance of important dissociation reactions such as



to produce elevated concentrations of atomic hydrogen. Calculations[59] of flowing plasmas with elevated electron temperatures have shown that increased dissociation of hydrogen is possible with moderate discharge currents and voltages. In the case of a recombining plasma approaching a water cooled substrate, energetic electrons can decrease the recombination rate of radical species (specifically atomic hydrogen) which have shown to be important in the diamond CVD process.

Diamond deposition experiments were performed in the DC arcjet facility (Figure 2.2) over a range of substrate biasing conditions while all other reactor conditions were held nominally constant. A hot-pressed boron nitride insulator was used on the substrate assembly to confine the discharge current and the deposition area to the 1.25 cm² area of the molybdenum rod. The secondary discharge was produced by a bank power supplies, capable of delivering a biasing voltage of up to +400 V to the deposition surface. The substrate temperature was monitored with an infrared optical pyrometer. The flow rates of the feed-gases for these experiments were 450 slpm of argon, 4.25% hydrogen in argon, and 2.44% methane in hydrogen. In the cases reported here the substrate temperature was maintained at 1125°C±25°C, and all the deposition times were one hour. Highly uniform films were deposited, covering the full area of the substrate.

The deposited films were measured for cross-sectional film thickness using scanning electron microscopy. A summary of growth rate as a function of current density through the secondary discharge can be seen in Figure 3.20. A factor of seven increase in the growth rate was observed with a significant bias current (4.9 cm² at 170 V) compared with the floating substrate case for these conditions. There appears to be a threshold current of ~2.4 A/cm² that must be reached in the secondary discharge before an increase in growth rate is observed. This threshold may be related to the energy required to increase the electron temperature to a critical value. At this point electron catalyzed reactions such as the one described above may become an important factor in controlling the amount of atomic hydrogen in the boundary layer and at the deposition surface.

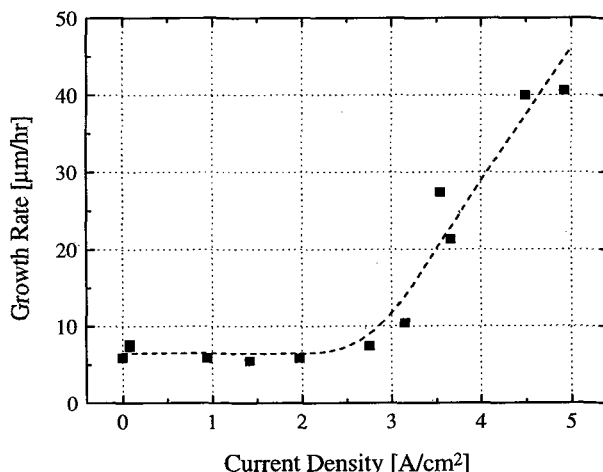


Figure 3.20 (♦) Growth rate of CVD diamond as a function of current density in the secondary discharge. (---) Approximate fit to the data.

Optical emission spectroscopy measurements have found that the electron temperature at the substrate is elevated above the freestream electron temperature when a potential is applied to the substrate. This indicates that the secondary discharge can be used to target the energy addition to the highly mobile free electrons in the plasma through joule heating.

Image processing was employed in this study to obtain a two-dimensional map of the emission from the first atomic hydrogen Balmer line (H_{α}). H_{α} emission is a result of an H atom decaying from its third to its second electronic energy level. This process emits a photon at a wavelength of 656.3 nm. A charge-coupled device (CCD), a lens system and a narrow band-pass interference filter centered at 656.3 nm were used to obtain images with and without a potential applied to the substrate. A computer analysis package acquired and analyzed the data for different biasing conditions. Figure 3.21 shows the results of the H_{α} imaging of the secondary discharge for a typical diamond growth experiment. The biasing conditions for this case were 5.1 A/cm² and 140 V across the secondary discharge. This image represents a 40 frame average with the potential applied to the growth surface after subtracting a 40 frame average without the potential applied. There is a large increase in H_{α} emission, particularly within the boundary layer, with a strong potential applied to the growth surface. The intensity of the H_{α} emission in this region was much brighter (by a factor of 5) than from the ~5000 K freestream. This may be an indication that the secondary discharge is significantly increasing the atomic hydrogen concentration in the boundary layer and flux to the substrate, leading to the higher growth rates observed.

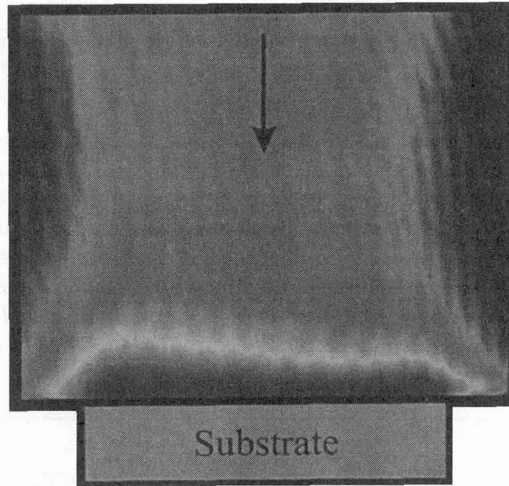


Figure 3.21 Two-dimensional image of the increase in the H_{α} emission due to the secondary discharge.

Raman analysis of each of the samples indicates very high quality films were deposited over the range of biasing conditions. Each of the spectra consisted of a sharp peak near 1332 cm⁻¹ with little or no amorphous carbon Raman signal. Figure 3.22 shows the Raman spectra for a diamond film deposited under a highly biased substrate condition (100 V and 2.76 A/cm²). The inset to Figure 3.22 is a high resolution scan and displays splitting of the 1332 cm⁻¹ diamond line (split ~4.3 cm⁻¹ in this case). In all the cases reported here, a full-width half-maximum (FWHM) of no more than 4.0 cm⁻¹ for the unshifted diamond component was measured, indicating high quality films were deposited. This splitting phenomena was typical of all the samples grown in this study, and has been attributed to high quality, highly oriented films that were stressed perpendicular to the growth direction (in-plane stresses).[64, 65] These in-plane, or anisotropic, stresses can arise in CVD diamond films during the cool-down period after the deposition process, and are caused by the mismatch in the thermal expansion coefficients of CVD diamond and the substrate material. The anisotropic stress shifts the Raman signal associated with

the crystal planes that are perpendicular to the growth direction while leaving the signal associated with the crystal plane in the growth direction unshifted. In the spectra, the higher wavenumber peak is attributed to the singlet mode and the lower wavenumber peak to the doublet mode of the Raman diamond line. These modes are normally degenerate in the absence of stress.[65]

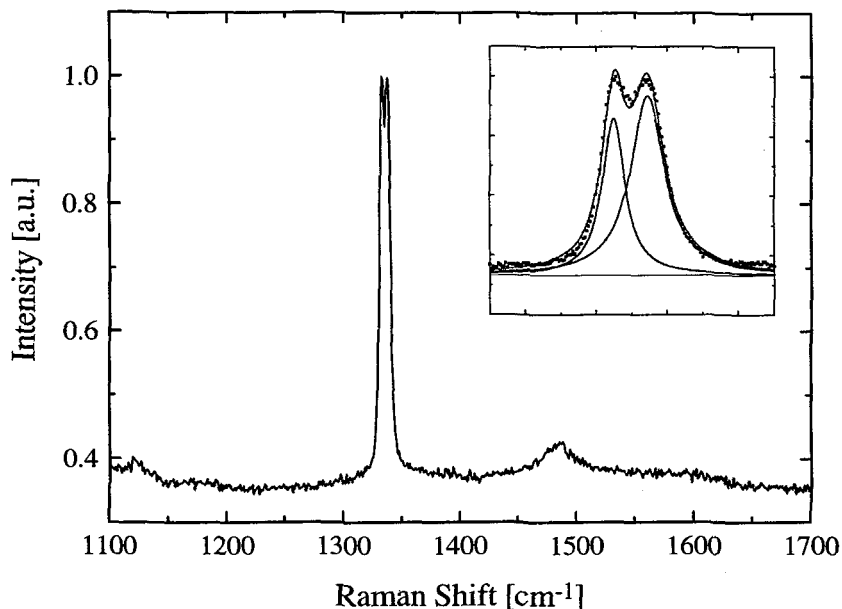


Figure 3.22 - Raman spectra of the deposited diamond film. Inset shows splitting of the 1332 cm^{-1} diamond peak.

These experiments indicate that a significant increase in growth rate of CVD diamond is possible with a positive potential applied to the growth surface. We observed that the growth rate increased by a factor of 7 when the deposition surface was biased at 170 V and 4.9 A/cm^2 as compared with the floating substrate case. The increased growth rate may be attributed to an increased flux of atomic hydrogen to the growth surface resulting from an elevated electron temperature that increased the near surface dissociation fraction of hydrogen. Imaging of the flow field found a significant increase in the H_{α} emission signal in the boundary layer over the deposition surface with a positive potential applied. Raman spectroscopy analysis indicated high quality films were deposited in all cases reported here. Splitting of the 1332 cm^{-1} Raman diamond line indicates highly oriented films that have a high degree of in-plane stresses.

4. CONCLUSIONS

Experimental investigations of atmospheric pressure plasma environments have demonstrated that the nonequilibrium behavior of these plasmas can be quite significant. The ability to understand nonequilibrium atmospheric pressure plasma systems and to apply them in plasma processing roles will rely on the accurate measurement of the plasma state and chemistry, and the ability to beneficially control the nonequilibrium state. Recent laser-based techniques have been demonstrated as powerful diagnostic tools, complimentary to traditional diagnostics of these environments, and initial experiments have shown great promise in the beneficial control of plasma chemical nonequilibrium for plasma CVD applications.

Acknowledgements

The authors would like to acknowledge the other members of our research group who have participated in these investigations: Dr. Scott Baldwin, Mr. Richard Gessman, Mr. Edward Wahl, and Mr. Maosheng Zhao. The authors would also like to acknowledge the organizations that have sponsored

the various research programs presented in this paper: the Department of Energy, Basic Energy Sciences (Grant #DE-FG03-88ER13957 under the direction of Dr. Oscar Manley), the Air Force Office of Scientific Research (Grant #F4962-94-1-0052 under the direction of Dr. Robert Barker), the Electric Power Research Institute (Grant #RP8042-05 under the direction of Dr. John Stringer), and the Engineering Research Center for Plasma-Aided Manufacturing (Grant #387P380 under the direction of Prof. J. Leon Shohet). The authors would also like to thank Prof. David G. Goodwin of Caltech for the use of his computational model.

References

- [1] T. G. Owano, M. H. Gordon, and C. H. Kruger, *Physics of Fluids B (Plasma Physics)*, vol. 2, pp. 3184-90, 1990.
- [2] T. G. Owano and C. H. Kruger, "Electron-Ion Three Body Recombination Coefficient of Argon," presented at the AIAA 22nd Fluid Dynamics, Plasma Dynamics & Lasers Conference, Honolulu, HI, 1991.
- [3] M. H. Gordon and C. H. Kruger, *Physics of Fluids B (Plasma Physics)*, vol. 5, pp. 1014-23, 1993.
- [4] G. M. W. Kroesen, D. C. Schram, C. J. Timmermans, and J. C. M. de Haas, *IEEE Transactions on Plasma Science*, vol. 18, pp. 985-91, 1990.
- [5] R. J. Kee and J. A. Miller, "A structured approach to the computational modeling of chemical kinetics and molecular transport in flowing systems," Sandia National Laboratory, Livermore, CA Report SAND86-8841, 1986.
- [6] D. K. Bohme, J. B. Hasted, and P. P. Ong, *Journal of Physics B (Atomic and Molecular Physics)*, vol. 1, ser.2, pp. 879-92, 1968.
- [7] C. Park, *Nonequilibrium Hypersonic Aerothermodynamics*. New York: Wiley, 1989.
- [8] M. H. Gordon and C. H. Kruger, "Ultra-Violet Recombination Continuum Electron Temperature Measurements in a Nonequilibrium Atmospheric Argon Plasma," presented at the AIAA 22nd Fluid Dynamics, Plasma Dynamics & Lasers Conference, Honolulu, HI, 1991.
- [9] S. C. Snyder, L. D. Reynolds, C. B. Shaw, Jr., and R. J. Kearney, *Journal of Quantitative Spectroscopy and Radiative Transfer*, vol. 46, pp. 119-24, 1991.
- [10] D. S. Baer, "Plasma Diagnostics with Semiconductor Lasers Using Fluorescence and Absorption Spectroscopy," Ph.D. Thesis, Stanford University, (1993).
- [11] C. O. Laux, R. J. Gessman, and C. H. Kruger, *AIAA Journal*, vol. 34, pp. 1745-1747, 1996.
- [12] M. G. Dunn and S.-W. Kang, "Theoretical and Experimental Studies of Reentry Plasmas," NASA CR-2232, April 1973 1973.
- [13] R. N. Gupta, J. M. Yos, R. A. Thompson, and K.-P. Lee, "A Review of Reaction Rates and Thermodynamic and Transport Properties for an 11-Species Air Model for Chemical and Thermal Nonequilibrium Calculations to 30,000 K," NASA RP-1232, August 1990 1990.
- [14] C. Park, *Journal of Thermophysics and Heat Transfer*, vol. 7, pp. 385-398, 1993.
- [15] C. O. Laux, R. J. Gessman, and C. H. Kruger, "Modeling the UV and VUV Radiative Emission of High-Temperature Air," presented at the 28th AIAA Thermophysics Conference, Orlando, FL, AIAA 93-2802, 1993.
- [16] C. O. Laux, T. G. Owano, M. H. Gordon, and C. H. Kruger, "Measurements of the Volumetric Radiative Source Strength of Air for Temperatures Between 5,000 and 7,500K," presented at the AIAA 5th Thermophysics and Heat Transfer Conference, AIAA 90-1780, 1990.
- [17] C. Park, "Nonequilibrium Air Radiation (NEQAIR) Program: User's Manual," NASA-Ames Research Center, Moffett Field, CA NASA-TM86707, 1985.
- [18] C. O. Laux, R. J. Gessman, and C. H. Kruger, "Mechanisms of Ionizational Nonequilibrium in Air and Nitrogen Plasmas," presented at the 26th AIAA Plasmadynamics and Lasers Conference, San Diego, CA, AIAA 95-1989, 1995.
- [19] R. J. Kee, F. M. Rupley, and J. A. Miller, "Chemkin-II: A Fortran Chemical Kinetics Package for the Analysis of Gas Phase Chemical Kinetics," Sandia National Laboratories, Livermore, CA, Report SAND89-8009, 1989.

- [20] G. V. Candler, C. O. Laux, R. J. Gessman, and C. H. Kruger, "Numerical simulation of a nonequilibrium nitrogen plasma experiment," presented at the 28th AIAA Plasmadynamics and Lasers Conference, Atlanta, GA, AIAA 97-2365, 1997.
- [21] H. Partridge, S. R. Langhoff, and C. W. Bauschlicher, *Journal of Chemical Physics*, vol. 88, pp. 3174-3186, 1988.
- [22] D. A. Levin, G. V. Candler, R. J. Collins, P. Erdman, E. Zipf, P. Espy, and C. Howlett, *Journal of Thermophysics and Heat Transfer*, vol. 7, pp. 30-36, 1993.
- [23] R. J. Gessman, C. O. Laux, and C. H. Kruger, "Experimental study of kinetic mechanisms of recombining atmospheric pressure air plasmas," presented at the 28th AIAA Plasmadynamics and Lasers Conference, Atlanta, GA, AIAA 97-2364, 1997.
- [24] T. G. Owano, C. H. Kruger, D. S. Green, S. Williams, and R. N. Zare, *Diamond and Related Materials*, vol. 2, pp. 661-666, 1993.
- [25] D. S. Green, T. G. Owano, S. Williams, D. G. Goodwin, R. N. Zare, and C. H. Kruger, *Science*, vol. 259, pp. 1726-9, 1993.
- [26] T. G. Owano, D. S. Green, E. H. Wahl, C. H. Kruger, and R. N. Zare, "Degenerate Four-Wave Mixing as a Spectroscopic Probe of Atmospheric Pressure Reacting Plasmas," presented at the 11th International Symposium on Plasma Chemistry, Loughborough, Leicestershire, England, 1993.
- [27] S. Williams, D. S. Green, S. Sethuraman, and R. N. Zare, *Journal of the American Chemical Society*, vol. 114, pp. 9122, 1992.
- [28] T. G. Owano, E. H. Wahl, C. H. Kruger, and R. N. Zare, "Degenerate Four-Wave Mixing as a Spectroscopic Probe of Boundary Layer Chemistry in Thermal Plasma CVD," presented at the 26th AIAA Plasmadynamics & Lasers Conference, San Diego, CA, AIAA 95-1954, 1995.
- [29] C. H. Kruger, T. G. Owano, and M. H. Gordon, *Journal of Pure and Applied Chemistry*, vol. 64, pp. 637, 1992.
- [30] D. G. Goodwin and G. G. Gavillet, *Journal of Applied Physics*, vol. 68, pp. 6393-400, 1990.
- [31] S. J. Harris, *Applied Physics Letters*, vol. 56, pp. 2298-2300, 1990.
- [32] M. Frenklach, *Journal of Chemical Physics*, vol. 97, pp. 5794-802, 1992.
- [33] S. S. Lee, D. W. Minsek, D. J. Vestyck, and P. Chen, *Science*, vol. 263, pp. 1596-8, 1994.
- [34] F. G. Celii, P. E. Pehrsson, H. t. Wang, and J. E. Butler, *Applied Physics Letters*, vol. 52, pp. 2043-5, 1988.
- [35] E. Villa, J. A. Dagata, J. Horwitz, D. Squire, and M. C. Lin, *Journal of Vacuum Science & Technology A (Vacuum, Surfaces, and Films)*, vol. 8, pp. 3237-40, 1990.
- [36] F. G. Celii and J. E. Butler, *Journal of Applied Physics*, vol. 71, pp. 2877-83, 1992.
- [37] E. J. Corat and D. G. Goodwin, *Journal of Applied Physics*, vol. 74, pp. 2021-9, 1993.
- [38] D. G. Goodwin, N. G. Glumac, and E. J. Corat, "Optical detection of CH₃ during diamond chemical vapor deposition," presented at the SPIE conference on laser techniques for state-selected and state-to-state chemistry, Los Angeles, CA, 2124, 1994.
- [39] N. Ota and N. Fujimori, "In situ detection of methyl radicals in filament assisted diamond growth environment by resonance ionization spectroscopy," presented at the Advanced in New Diamond Science and Technology, MYU, Tokyo, Japan, 1994.
- [40] M. A. Childs, K. L. Menningen, P. Chevako, N. W. Spellmeyer, L. W. Anderson, and J. E. Lawler, *Physics Letters A*, vol. 171, pp. 87-9, 1992.
- [41] H. Toyoda, M. A. Childs, K. L. Menningen, L. W. Anderson, and J. E. Lawler, *Journal of Applied Physics*, vol. 75, pp. 3142-50, 1994.
- [42] W. L. Hsu, *Applied Physics Letters*, vol. 59, pp. 1427-9, 1991.
- [43] S. J. Harris and A. M. Weiner, *Journal of Applied Physics*, vol. 67, pp. 6520-6, 1990.
- [44] E. Kondoh, T. Ohta, T. Mitomo, and K. Ohtsuka, *Journal of Applied Physics*, vol. 72, pp. 705-11, 1992.
- [45] E. Kondoh, T. Ohta, T. Mitomo, and K. Ohtsuka, *Diamond and Related Materials*, vol. 3, pp. 270-6, 1994.
- [46] D. Romanini and K. K. Lehmann, *Journal of Chemical Physics*, vol. 99, pp. 6287-301, 1993.
- [47] P. Zalicki and R. N. Zare, *Journal of Chemical Physics*, vol. 102, pp. 2708-17, 1995.

- [48] A. O'Keefe, J. J. Scherer, A. L. Cooksy, R. Sheeks, J. Heath, and R. J. Saykally, *Chemical Physics Letters*, vol. 172, pp. 214-18, 1990.
- [49] T. Yu and M. C. Lin, *Journal of the Americal Chemical Society*, vol. 115, pp. 4371, 1993.
- [50] G. Meijer, M. G. H. Boogaarts, R. T. Jongma, D. H. Parker, and A. M. Wodtke, *Chemical Physics Letters*, vol. 217, pp. 112-16, 1994.
- [51] Y. A. Mankelevich, A. T. Rakhimov, and N. V. Suetin, *Diamond and Related Materials*, vol. 4, pp. 1065-8, 1995.
- [52] Y. A. Mankelevich, , 1996.
- [53] D. G. Goodwin, *Journal of Applied Physics*, vol. 74, pp. 6895-906, 1993.
- [54] D. G. Goodwin, *Journal of Applied Physics*, vol. 74, pp. 6888-94, 1993.
- [55] J. C. Angus and C. C. Hayman, *Science*, vol. 241, pp. 913-921, 1988.
- [56] S. K. Baldwin, Jr., T. G. Owano, and C. H. Kruger, *Plasma Chemistry and Plasma Processing*, vol. 14, pp. 383-406, 1994.
- [57] B. W. Yu and S. L. Girshick, *Journal of Applied Physics*, vol. 75, pp. 3914-23, 1994.
- [58] C. H. Kruger, "Nonequilibrium effects on thermal plasma chemistry," presented at the The 8th International Symposium on Plasma Chemistry, Tokyo, Japan, 1987.
- [59] C. H. Kruger, *Plasma Chemistry and Plasma Processing*, vol. 9, pp. 435-43, 1989.
- [60] S. Matsumoto, I. Hosoya, and T. Chounan, *Japanese Journal of Applied Physics*, vol. 29, pp. 2082-2086, 1990.
- [61] S. Matsumoto, I. Hosoya, Y. Manabe, and Y. Hibino, *Pure and Applied Chemistry*, vol. 64, pp. 751-758, 1992.
- [62] S. Yugo, T. Kanai, T. Kimura, and T. Muto, *Applied Physics Letters*, vol. 58, pp. 1036-1038, 1991.
- [63] B. R. Stoner, G. H. M. Ma, S. D. Wolter, and J. T. Glass, *Physical Review B*, vol. 45, pp. 11067-11084, 1992.
- [64] M. H. Loh, J. G. Liebeskind, and M. A. Cappelli, "Arcjet thrusters for the synthesis of diamond and cubic-boron nitride films," presented at the 30th AIAA/ASME/SAE/ASEE Joint Propulsion Conference, Indianapolis, IN, AIAA 94-3233, 1994.
- [65] S. A. Stuart, S. Praver, and P. S. Weiser, *Applied Physics Letters*, vol. 62, pp. 1227-1229, 1993.